Draft version December 23, 2024
Typeset using LaTeX default style in AASTeX631

Impacts of The Metagalactic Ultraviolet Background on Circumgalactic Medium Absorption Systems

Elias Taira [1], Claire Kopenhafer [2,1], Brian W. O'Shea [3,1,4,2], Alexis Rollins,[5] Evelyn Fuhrman,[1] Molly S. Peeples [6,7], Jason Tumlinson [6,7] and Britton D. Smith [8]

[1] Department of Physics & Astronomy, 567 Wilson Road, Michigan State University, East Lansing, MI 48824
[2] Institute for Cyber-Enabled Research, 567 Wilson Road, Michigan State University, East Lansing, MI 48824
[3] Department of Computational Mathematics, Science, & Engineering, Michigan State University, 428 S. Shaw Lane, East Lansing, MI 48824
[4] Facility for Rare Isotope Beams, Michigan State University, 640 S. Shaw Lane, East Lansing, MI 48824
[5] Department of Physics & Astronomy, Gallalee Hall, University of Alabama, Tuscaloosa, AL 35401
[6] Space Telescope Science Institute, 3700 San Martin Dr., Baltimore, MD 21218
[7] Center for Astrophysical Sciences, William H. Miller III Department of Physics & Astronomy, Johns Hopkins University, 3400 N. Charles Street, Baltimore, MD 21218
[8] Institute for Astronomy, University of Edinburgh, Royal Observatory, EH9 3HJ, UK

ABSTRACT

[CK: I'll admit I sort of gave up reading the abstract and focused on the text. It's not worth nitpitcking the abstract in my opinion until the rest of the text is more concrete.] [BWO: Agreed, let's come back to this later.] Among the many different pieces of physics that go into simulations of the circumgalactic medium (CGM), the metagalactic ultraviolet background (UVB) is notable in that it plays a significant role in the ionization of different species but is not fully understood. At this point in time, there are a variety of UVB models that have been created based on the quantity / intensity of different ultraviolet sources (i.e. stars and quasars). In this project, we perform pairwise comparisons of the ionization patterns of four different UVB models, specifically looking at how these models impact the ion column densities of individual gas clouds in the CGM. From our analysis we find evidence that shows UVB models produce significant changes in the ionization, but these differences are specific to the models' design and will require further investigation.

1. INTRODUCTION

Claire's text changes [CK: Claire's notes]

Brian's text is in this color. [BWO: Brian notes look like this]

The circumgalactic medium (CGM) is the diffuse, multiphase medium that surrounds a galaxy. It is typically observed via quasar absorption spectra due to its overall low surface brightness. Such observations have been gathered in a number of observational surveys, including COS-Halos (Tumlinson et al. 2013), COS-Burst (**?**), the COS CGM Compendium (Lehner et al. 2018), KODIAQ and KODIAQ Z (Lehner et al. 2014; Lehner et al. 2016; Lehner et al. 2022), Red Dead Redemption (Berg et al. 2019), CASBaH (Burchett et al. 2018; Prochaska et al. 2019), CUBS (Chen et al. 2020), CGM2 (Wilde et al. 2021).These surveys have resulted in absorption estimates for a wide range of metal ions which can then be used to extract information about the physical properties of the CGM such as its multiple gas densities, temperatures, and metallicities.

To better understand the history of the CGM and its evolution over time, a large suite of simulations have been developed. This work includes cosmological simulation studies of the CGM absorption structure such as: EAGLE (Wijers et al. 2020), GIBLE (Ramesh et al. 2024), Illustris-TNG50 (DeFelippis et al. 2021), FOGGIE (Zheng et al. 2020), and Hummels et al. (2019) as well as some idealized simulations: Fielding et al. (2017) and Butsky et al. (2022). It is vital that these experiments study metal ion distributions to effectively compare the results of these simulations with observation.

Conceptually, there are two broad frameworks for connecting absorption spectra with physical gas properties: forward and reverse modeling. Taking the physical properties of the CGM as the underlying "ground truth," reverse modeling must be applied to observations in order to "back out" the underlying gas state from the observed spectra. The absorption spectrum represents a reduced set of information about the system that generated it and such a situation is also known as an "inverse problem" (see, e.g., Yaman et al. 2013). Conversely, efforts to make synthetic observations

of simulations are engaging in forward modeling. Synthetic observations can go as far as generating mock spectra targeting a specific instrument (such as the Hubble Telescope's Cosmic Origins Spectrograph) complete with noise (Hummels et al. 2017). For spectral observations of metal ions, the two approaches can "meet in the middle" by generating column densities of specific ions. Column densities can be reversed modeled from spectral line features and forward modeled from bulk gas properties. While simulations could in theory directly model individual metal ion densities—thereby removing the need to forward model ionic column densities—this is computationally intractable. It is already quite uncommon to track individual element densities (the notable exception being EAGLE; Schaye et al. (2014)) much less individual ion densities. Therefore, inferring elemental and ionic gas fractions must be part of the forward modeling process.

Connecting ionic absorption and gas properties through either forward or reverse modeling involves several assumptions. In recent years there has been considerable effort invested in characterizing the uncertainties that these assumptions introduce into reverse modeling. For instance, to extract physical data from absorption spectra, it is commonly assumed that each absorption feature originates from a single gas "cloud" or "clump" along the line of sight. Instead, Haislmaier et al. (2020) showed that multiple line components may be needed to accurately capture the information contained in an absorption feature. Single component analysis is only capable of reproducing the average metallicity of multiphase structures (Marra et al. 2021) while multiple spatially distinct clumps can contribute to the same observed absorption feature if they overlap in line-of-sight velocity space (Marra et al. 2022).

While it is likely not always true, for both forward and reverse modeling it is assumed that CGM gas is in ionization equilibrium; that is, that individual ions are in both collisional and photoionization equilibrium. In particular, the assumption of photoionization equilibrium requires that we understand the nature of the metagalactic ultraviolet background (UVB)—the background radiation originating from quasars and newly-formed stars. However, the UVB is challenging to model as it requires its own broad assumptions about extragalactic star formation rates and the distribution of quasars throughout the universe and across cosmic time. Indeed, the UVB itself is an abstraction representing the *average* UV radiation field at a point in space far from any single galaxy. Because of these challenges, many models for the metagalactic UVB have been created over the past few decades. This makes the UVB a potential source of uncertainty in the models that connect spectral observations and their underlying gas.

Again, there has been effort in quantifying how much uncertainty the UVB contributes to the reverse modeling of absorption spectra. Both Gibson et al. (2022) and Acharya & Khaire (2022) have studied how the extreme-UV (EUV) portion of the UVB ($\approx$ 1–1000 Ryd) affects inferences of number density and metallicity. The former finds that hardening the EUV slope from $\alpha_{\rm EUV} = -2.0$ to -1.4. causes the metallicity to increase by an average of 3 dex. The latter found that the number density and metallicity could vary by factors of 6.3 and 3.7 in low density gas ($\approx 10^{-5}$ cm^{-3}) and 3.3 and 2.2 in high density gas ($\approx 10^{-3}$ cm^{-3}).

Though understanding model uncertainty is a necessary process, it is important to reiterate that efforts have so far been focused on the implications for reverse modeling. Forward modeling from simulations is extremely valuable for comparing simulations and observations so it is imperative that we quantify the uncertainty introduced by common, necessary assumptions to the forward modeling process. As a start to this process, the goal of the work presented here is to quantify the variation in absorber column density introduced by uncertainties in the metagalactic ultraviolet background. We do this by repeatedly post-processing cosmological simulations from the FOGGIE project (Peeples et al. 2019; Simons et al. 2020) with a pipeline that is identical except for the choice of metagalactic UVB. We then match clumps between each post-processing pass based on their physical location in order to compare the forward modeled column densities and underlying volumetric densities and temperatures. In Section 2, we discuss our data selection, simulation pipeline, and general methodology for performing our analysis, including the algorithm for matching clumps. In Section 3, we present the results of our analysis, and in Section 4, we interpret our findings and discuss the implications of our results in the broader research community. Finally, we summarize our findings and discuss possibilities for future research project in Section 5.

2. METHODOLOGY

For clarity, we present our process in the form of a flowchart that summarizes our data analysis pipeline in Figure 1. Each block of the figure corresponds to a subsection below. We base our analysis on the FOGGIE simulations (Section 2.1, Peeples et al. (2019); Simons et al. (2020)). We use the Synthetic Absorption Line Surveyor Application (SALSA; Boyd et al. 2020) to cast lines of sight or "rays" within a specified range of impact parameters (Section 2.2). SALSA is built on Trident, a synthetic absorption spectra tool (Hummels et al. 2019) that is used by SALSA to estimate ion

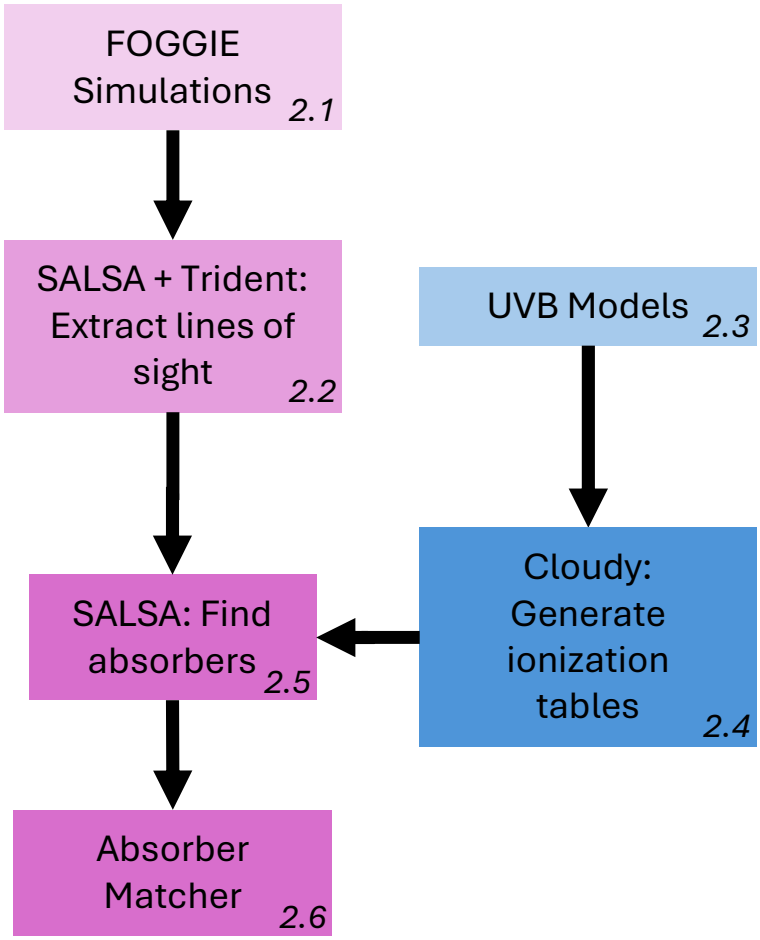

Figure 1: Overview of the analysis pipeline used in this work

. Each block represents a different calculation and/or data product, as detailed in the following subsections. In the bottom right corner of each box is the section that each block corresponds to. [BWO: I suggest making this figure go left-to-right instead of vertically, it makes better use of space and is easier to read.]

column densities. Trident is itself built on yt (Turk et al. 2011), which it uses to load the FOGGIE simulation data. The number densities inferred by Trident are used by SALSA to find absorbers within each ray and calculate their column density and other properties.

We adopt four different metagalactic ultraviolet backgrounds as outlined in Section 2.3 and, using SALSA, find a set of absorbers for each. For each set of SALSA absorbers created from each UVB, we match the absorbers based on their spatial position along the line of sight so that pairwise comparisons can be made.

2.1. *The FOGGIE Simulations*

The FOGGIE (Figuring Out Gas and Galaxies In Enzo) Galaxies are a suite of cosmological zoom-in simulations of Milky Way-like galaxies that were made using Enzo. One defining feature of the FOGGIE simulations is its high spatial and mass resolution in the circumgalactic medium, allowing for a more precise analysis of this region than in typical cosmological simulations. This is also the main reason we selected these galaxies for our study [BWO: Why just refer to these two papers? Also refer to FOGGIE website[1].] (Peeples et al. 2019; Simons et al. 2020). We base

[1] Also see the FOGGIE website at https://foggie.science

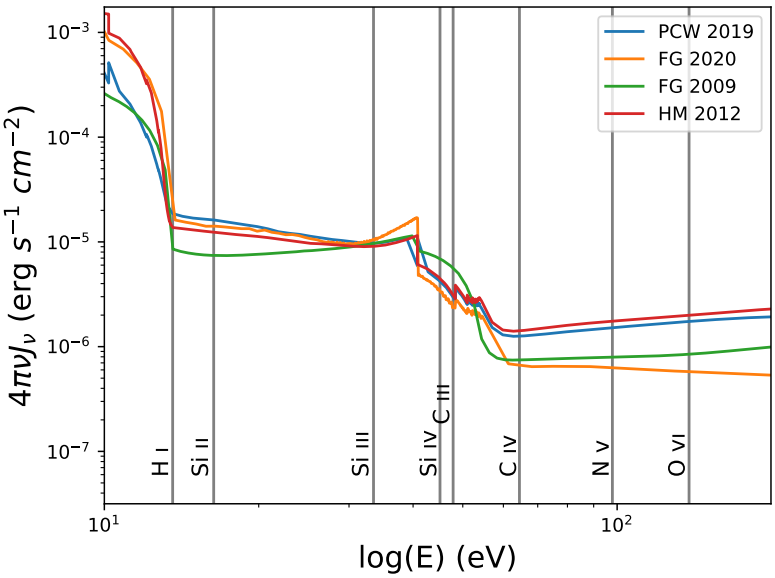

Figure 2: Indicates the energy distribution of two of the newest UVB models at redshift 2.5, FG 2020 and PCW 2019. The x-axis is the energy of the UVB in units of eV and the y-axis is the intensity of the UVB in units of $ergs^{-1}cm^{-2}$. [BWO: Need to tighten up the y-axis and make lines thicker, text larger so it's easy to see. I think we also ought to make a data table with all of this information and make it publicly available – people will really appreciate it and refer to the paper!]

our analysis on the Hurricane galaxy at redshift 2.5, during cosmic noon when the intensity of UV radiation is very high due to the high cosmic star formation rate density, and thus when one might reasonable expect that the impact of variations in the UVB might be largest. [BWO: At various places later in the paper you refer to "redshifts" and "galaxies", but as far as I can tell we're really only using a single data output of a single galaxy. This needs to be fixed.]

One limitation of the FOGGIE simulations, however, is that they only follow the evolution of a single "metal field," in which all of the CGM metals are tracked assuming constant abundance ratios (though variable magnitudes), ignoring traces of individual species of ions. This then necessitates some form of post-processing method to extract data for these untracked ions.

2.2. *Extracting Lines of Sight*

We use SALSA to mimic observations by generating a series of randomly oriented lines of sight, or "rays," through the CGM. SALSA calculates random start and end points for our rays given a central point, ray length, and a range of impact parameters. This lets us approximate observational sightlines passing within a certain distance (i.e., impact parameter) of the galaxy center. [CK: Our central point corresponds to peak of the halo dark matter distribution. What are the values of the length and impact parameter bounds? Claire TODO: report the virial radius of the halo (we want to make it clear that we're actually looking at the CGM, not the ISM or IGM!).] In this way, we generate 100 rays through our simulated galaxies. These same 100 rays will be reanalyzed using different UV backgrounds (Section 2.3.

With the spatial orientation of the rays specified by SALSA, Trident is used to infer the ionic number densities using CLOUDY-generated equilibrium ion fraction tables(see Section 2.4) using the following equation: $n_{X_i} = n_X f_{X_i}$, where n_X is the total number density of the element as determined by the elemental abundances, which, in the case of this work we elect to use Solar abundance patterns. f_{X_i} is the equilibrium fraction of a given ion, and n_{X_i} represents the inferred ion number density (Hummels et al 2018).

2.3. *UVB Models*

We use two different "families" of metagalactic ultraviolet background models with two models each for a total of four UVB models in total. These families are Faucher-Giguère et al. (2009) and Faucher-Giguère (2020) (FG09 and FG20 respectively, and Puchwein et al. (2019) (PW19) and Haardt & Madau (2012) (HM12). These models were selected both to allow us to analyze the differences between model families and the differences between model generations of models within a single family. PCW 2019 was developed in response to new photoionization and photoheating rates being determined by Oñorbe et al. (2017) as well as new calibrations to their effective rates to reach a higher optical depth ($\tau_e = 0.065$) to match the Plank 2015 observations (Faucher-Giguère 2020). For FG 2020, they make a number of updates based on updated galaxy UV luminosity functions, a new stellar spectral template, new AGN luminosity functions, improved IGM opacity measurements, updated Ly α forest constraints, Plank 2018 reionization constraints, and, finally, updated observational constraints on He IIreionization (Faucher-Giguère 2020).

In Figure 2, we show the intensity spectra (in units of $erg\ s^{-1}\ cm^{-2}$) of all four UVBs that we use in this work. Each of the vertical black lines represents the ionization energies (in eV) of each of the ions used in this study, the list of which is as follows: H I, Si II, Si III, C III, Si IV, C IV, N V, O VI. We include Si II to Si IV to evaluate the effect of the UVB for different ionization states of an element. C III is used as its ionization state is in a region of the spectra that is changing very rapidly, compared to Si IV which has a very similar ionization state, may help reveal the effects of the nonlinear portion of the spectra on column density. As for C IV, N V, and O VI, they are included due to their observational significance. C IV, is useful for tracing CGM cold gas.

2.4. *CLOUDY Ionization Tables*

As seen in Equation 1, the UVB is coupled to the pipeline through equilibrium ionization fractions, f_{X_i}. We use CLOUDY to generate a table of these fractions for a broad range of densities, temperatures, and metallicities. Both the FG09 and HM12 models have ionization fraction tables available as part of the Trident project [2]. The newer FG20 and PW19 models do not have readily available tables made for them. To generate tables for these UVBs, we ran a series of one-zone CLOUDY models to determine the equilibrium ionization fractions for selected elements (see Section 2.3 for list). These models include self-shielding and were coordinated using the same code as the older FG09 and HM12 models [3]. Britton's Cloudy Cooling Tools are not widely known nor do they have a reference, so we don't need to name drop them. Including a footnote with the github link is good though. [BWO: We also should make the HDF5 files for the UVBs publicly available - maybe contribute them back to Trident?]

2.5. *Absorber Extraction*

Once Trident has inferred ionic number densities using the CLOUDY ionization fraction table corresponding to one of our four UVBs, SALSA is able to identify absorbers within the rays it randomly placed (Section 2.5). SALSA does this iteratively for each individual ion using the Simple Procedure for Iterative Cloud Extraction (SPICE) method. A key assumption of this algorithm is that regions of high column density should give rise to detectable absorption features.

This algorithm works by setting an ion number density threshold above which lies some fraction of the ray's total column density of the ion in question. By default, the cutoff is 0.8 Then, bounds are set that define distinct "clumps" of gas that fall above this cutoff. That is, regions of space are identified that account for 80% of the total column density of that ion. On the next pass, additional regions are flagged that account for 80% of the column density that remains unaccounted for after the first pass. Clumps from each pass are combined if their average line-of-sight velocities are within 10 km/s of each other. This process is repeated until the column density of the remaining data that has not been assigned to an absorber is below the minimum density threshold. Therefore, the SPICE algorithm is controlled by two free parameters: the cutoff fraction and the minimum column density.

To ensure our results are not sensitive to these two free parameters, we employ a pseudo-grid search to determine the optimal set of parameters to apply to this algorithm. We track the distribution of $\log(N_{\mathrm{H\ I}})$ for absorbers found by independently varying both parameters. The parameter not being analyzed is left at its default setting (0.8 for the cutoff fraction and 10^{13} cm^{-2} for the minimum column density). It should be noted that we did not investigate the non-linear effects from varying both settings at once. Our aim is to find a parameter space in which we find a "stable" region in parameter-space in which the distribution does not shift significantly between different parameter settings. [BWO: The preceding sentence does not really make sense. Please reword it!]

[2] https://trident-project.org/data/ion_table/

[3] https://github.com/brittonsmith/cloudy_cooling_tools

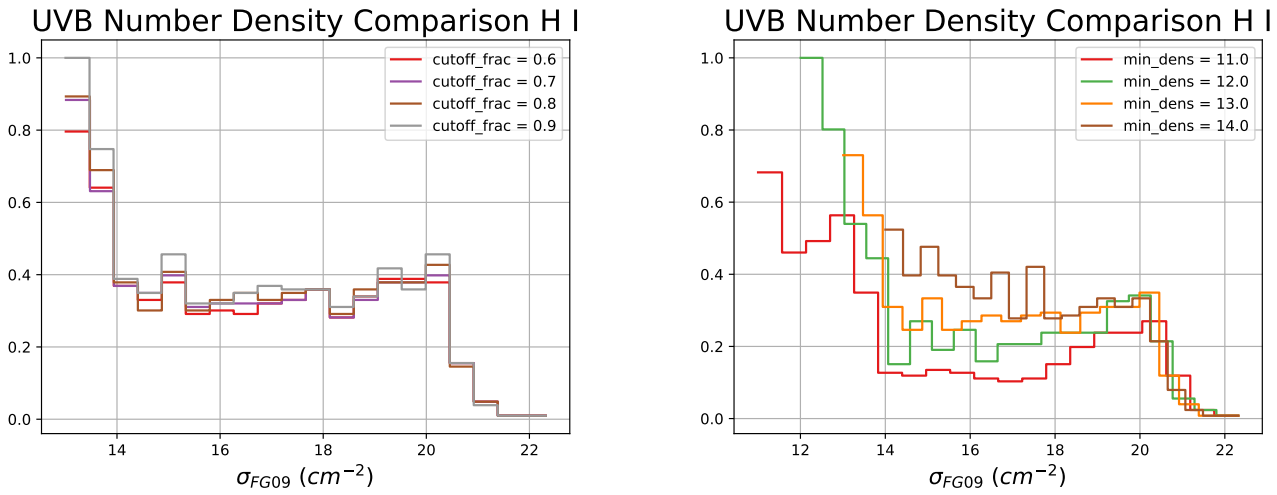

(a) (b)

Figure 3: (a) A histogram showing the column density of SALSA absorbers produced using the SPICE method with cutoff fractions from 0.6–0.9 in intervals of 0.1. (b) A histogram of SALSA absorbers produced at different minimum density thresholds from $\log(N) = 11.0$–14.0 in intervals of $\log(N) = 1$. [BWO: Remove figure titles. Make data lines thicker (they're currently comparable to the underlying grid). Make underlying grid lower opacity. Label y axis. Make it clear X-axis is log. Also note that this figure is throwing LaTeX errors.]

Figure 3, we plotted a histogram showing H I column densities of SALSA absorbers for two different SALSA settings: cutoff fraction (Fig. 3a) and minimum density (Fig. 3b). For our cutoff fraction distributions in Fig. 3a, we select four different settings including the default fraction of 0.8, from 0.6-0.9 in intervals of 0.1 while the minimum density cutoff remains at $log(N) = 13.0\ cm^{-2}$. In Fig. 3b, the minimum column density cutoff is plotted at four different settings, including the default minimum column density setting, ranging from $\log(N) = 11$–14 in intervals of $\log(N) = 1$.

From our variation of the cutoff fraction in panel (a) of Figure 3, we find that the overall distribution remains generally consistent despite the different settings used. Even though the total number of absorbers that SALSA identifies steadily decreases with increasing cutoff fraction, this decrease is small relative to the total number of absorbers found. This indicates that the cutoff fraction does not have a significant impact on the results of our analysis, so we elected to leave this parameter at its default value of 0.8. In panel (b) of Figure 3 we see that as the minimum column density parameter increases the total number of absorbers detected decreases rapidly, with the overall H I column density distribution skewing towards higher column densities. Unlike with the cutoff fraction, the H I column density distribution does not remain stable as we vary the minimum column density. Instead, we chose to adopt different minimum column densities for each ion of interest. For H I, C III, C IV, and O VI we use $log(N) = 12.5$. For Si IIand Si III, we use $log(N) = 11.5$. Finally, for N V, we use $log(N) = 13.0$. We select these values based on the minimum column density these absorbers could potentially be detected by observation (Tumlinson et al. 2011; Tumlinson et al. 2013; Werk et al. 2013, 2016; Bordoloi et al. 2014; Bordoloi & Longmire 2018; Lehner & Howk 2011) [BWO: Combine all of these references into a single large citep citation]

Once SALSA has identified absorbers for each ion based on their number density it reports gas properties such as volumetric density, temperature, and metallicity for each absorber. These quantities are a column density-weighted average of the cells belonging to that absorber.

2.6. *Absorber Matching*

The UVB will affect the ion number densities of the ray and therefore the clumps identified by the iterative SPICE algorithm. Once the SPICE algorithm has been run on our 100 rays for each of our four UVBs, we must match absorbers based on their position along each line of sight. This is because our analysis relies on pairwise comparison between absorbers from different UVBs. Altering the UVB and overall ion number density can change the shape of

the identified absorbers, so we categorize them into different groups based on their relative size and position along a given ray. The categories are as follows:

1. Match: absorbers are of the exact same size and position along the ray, covering the same resolution elements in the underlying cosmological simulations.

2. Different Size: the two absorbers are different sizes (i.e., they span a differing number of underlying simulation cells) but match in either start or end position. In other words, one UVB results in a clump that is longer or shorter than that from another UVB, but they still occupy the same physical region along the ray.

3. Overlap: absorbers have a significant overlap with one another along the line of sight, but they do not fully line up in terms of size or position (i.e., they do not share a start or end point and thus are likely to encompass a different number of cells).

4. Merge: when one of the UVBs produces multiple small absorbers but the other UVB produces only one large absorber that is a superset of the smaller ones and spans the same spatial extent.

5. Lonely: there exists an absorber in one UVB while the other UVB has no absorber.

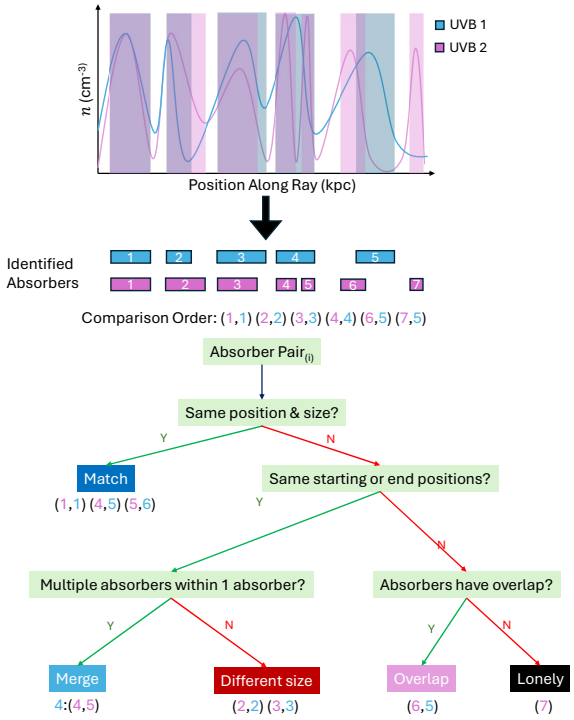

Figure 4: Diagram showing a flow chart of how the pairwise comparison algorithm. Each absorber is numerically labeled in the order they appear along the ray. The "comparison order" list indicates the order in which pairs of absorbers are put through the flow chart.

All of these comparisons are made using a series of Boolean comparisons with some margin of error allowed. We apply a margin of error in this case to prevent situations in which compared absorbers are misclassified. Specifically, this is to prevent situations in which, for example, a pair of absorbers would fall into the Different Size category when the size of the two absorbers is only a one-cell difference. It is also to prevent situations in which absorbers would

be classified as Lonely when the two absorbers are only a few cells apart from one another and thus still viable for comparison. [BWO: In this previous sentence to you mean that the absorbers have no spatial overlap, or just that it's very small?]

Specifying a margin of error in terms of cells is difficult for this analysis as the ray can have a variable path length *dl* through each cell in the underlying simulation, even if those cells have uniform spatial resolution. To address this issue we adjust the margin of error such that it has the lowest number of absorber pairs that are classified as 'match' that exist outside the general trend of the data

This hinges on the assumption that absorbers that share similar spatial coordinates have similar physical quantities (i.e., gas density, temperature, and metallicity). Using this method, we determined through experimentation that 7 simulation cells along the line of sight was the optimal margin of error. [BWO: You should mention here how many cells are typically in an absorber – is seven a large number or a small number in comparison to that? So, is this a small tweak or a big tweak?]

In order to compare absorber properties across UVBs, the small individual clumps in Merge cases had their properties combined in linear space. [BWO: what do you mean by "in linear space" here? Please explain.] As for the other physical quantities of the absorber, such as temperature and gas density, (see Section 2.5) these were combined by weighted average based on the column densities of the individual absorbers in the following equation:

$$\overline{x} = \frac{x \cdot \sigma}{\sum_{i=1}^{n} N_i}$$

where $\overline{x}$ is the weighted average quantity, n is the number of absorbers within the set being combined, x is the array of a given physical quantities of length n, σ is the array column densities also of length n, and N_i is the number density of a given absorber.

Lonely cases were removed from the analysis as they have no partner to compare to. We found that the number of such absorbers was small. The fraction of lonely absorbers is $\simeq 1\%$ for each pairwise comparison (i.e., for each pair of UVBs that are compared). [BWO: I am assuming that's what you meant by pairwise comparison; please change if the new parenthetical is incorrect.]

Additionally, there were a few rays for which the sorting algorithm was unable to categorize absorber pairs. These cases consisted of absorbers that fell into multiple categories, or rays that had no absorbers. [CK: Is this because of our margin of error? I would otherwise think our categories are mutually exclusive.] Instead of attempting to develop categories for all of these outliers, the rays are removed from the analysis. The number of removed rays tends to stay around 0-10% for most ions. However for N V, 37-68% are removed from the analysis depending on which pair of UVBs are compared. This is mostly due to the fact that the abundances of this nitrogen ion are significantly lower than the other ions used in this work. Thus, SALSA recognized many of the N V rays as having no observable absorbers.

[CK: Once you make the table of total absorber counts for each UVB, describe it and reference in a paragraph here, at the end of this subsection]

3. RESULTS

Using the methodology described in Section 2 we make three pairwise comparisons: FG09 and FG20 (Faucher-Giguère family), HM12 and PW19 (Haardt-Madau-Puchwein family), and finally FG20 and PW19, the latest models from each family. We begin by comparing the total column densities along each ray and then perform a comparison between individual absorbers and their physical properties as identified by the pipeline described in Section 2.

Figure 5 shows a comparison between the total column densities between each of the three pairwise model comparisons for each ion considered in this work, plotting the average $\bar{N}$ in the x-axis, along with the log difference between the two UVBs in the y-axis. The points in purple refer to the comparison between FG20 and FG09 ($\log \frac{FG20}{FG09}$), the magenta points refer to PW19 and HM12 ($\log \frac{PW19}{HM12}$), and the orange to PW19 and FG20 ($\log \frac{PW19}{FG20}$). Additionally, there is also a line plotted for each comparison indicating the moving average of the data with a window size of 20 rays. The different ions used in the comparison are ordered in terms of increasing ionization potential from left to right.

Throughout each comparison, we find that the FG20 and FG09 models tend to have the best agreement, with differences between the two UVBs never being larger than $\simeq 0.75$ dex for any ion. These differences also tended to be consistent for the entire density range (that is, the scatter would exist entirely above or below the zero-line with very little exception), reflecting systematic differences in the species densities resulting from the two UVBs. The PW19/FG20 comparison saw much larger differences. Starting in the H I panel (top left), in the region between

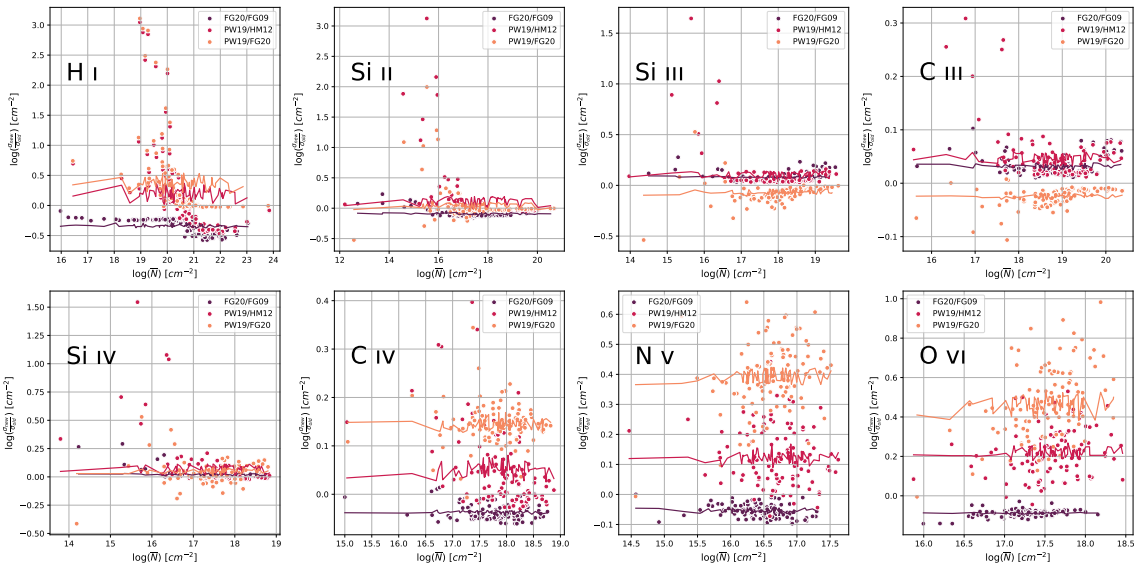

Figure 5: Differences in total column density along the line of sight as different UVBs are applied. Differences are quantified as $\log(N_{\rm new}/N_{\rm old})$, the ratio between new and old UVBs as listed in the figure legend. Quantities on the x-axis are the average of the total column densities between the two UVBs in the comparison (written $\log(\bar{N})$). The points in purple refer to the comparison between FG20 and FG09 ($\log \frac{FG20}{FG09}$), the magenta points refer to PW19 and HM12 ($\log \frac{PW19}{HM12}$), and the orange to PW19 and FG20 ($\log \frac{PW19}{FG20}$). Additionally, there is also a line plotted for each comparison indicating the moving average of the data with a window size of 20 rays. The different ions used in the comparison are ordered in terms of increasing ionization energies from left to right. [BWO: Axis labels are too small to read. The key in each panel is identical; just plot it once (top left is fine) and state in the caption that it's duplicated. Please smooth out the lines you've plotted a bit more so that they are less busy-looking. You say in the caption that they're smoothed over a window size of 20 rays but it doesn't look like it... I would also suggest making a note in the caption that the x- and y-axis scales are all different.]

$log\overline{N} = 19 - 20$ the amount of H I in PW19 rays is significantly larger than in the HM12 rays by up to a factor of $\simeq 10^3$ (but only for rays with total clumn densities in this narrow range). In the Si II panel there is a similar feature from $log\overline{N} = 14 - 16$. This appears to be significantly less pronounced than the feature observed in H I however, and in Si III and Si IV this feature appears to be even less pronounced (though still reaching differences of $\simeq 10^{1.5}$ in some small fraction of cases). This feature is also present in the PW19/FG20 comparison in the H I panel, almost perfectly aligning with the P19/HM12 comparison. Unlike in the P19 vs. HM12 comparison, in the PW19 vs. FG20 comparison this feature is significantly less pronounced in Si II – though it appears in a similar range of $log\overline{N} = 14-16$, the largest difference is only a factor of 10^2. In ions with higher ionization potentials this feature does not persist.

[BWO: I totally rewrote the summary for this figure. Given that none of the other figure descriptions used bullet points I got rid of it here as well.] Looking at the differences between pairwise comparisons of total ion column densities in Figure 5, we find that the differences between UVBs display distinct trends. The total H I column densities have notable systematic offsets (with a typical offset of $\simeq 0.3$ dex between pairs of models), with very large differences in total column densities between compared sight lines for a narrow range of total column densities. Si II, Si II, C III, and Si IV have a very strong agreement between their distributions with very small typical offsets between UVBs (generally $\simeq 0.1$ dex), although a small fraction of the sightlines (particularly those with low total column densities) have notable differences. C IV, N V, and O VI display significant offsets between models (particularly when comparing the PW/HM vs. FG families of models) as well as significant scatter within those offsets. This offset and scatter generally grows with increasing ionization potential.

[BWO: Discussion of Figure 6 would go here!]

Figure 7 shows the column density differences between individual FG09 and FG20 absorbers found using the SALSA algorithm and their relationship with different physical quantities in the simulation data. The column density difference is $\log \frac{FG09}{FG20}$. In order from left to right, the quantities are: FG09 absorber column densities (column 1), absorber gas density (column 2), temperature (column 3), and finally a histogram of the column density differences in the rightmost

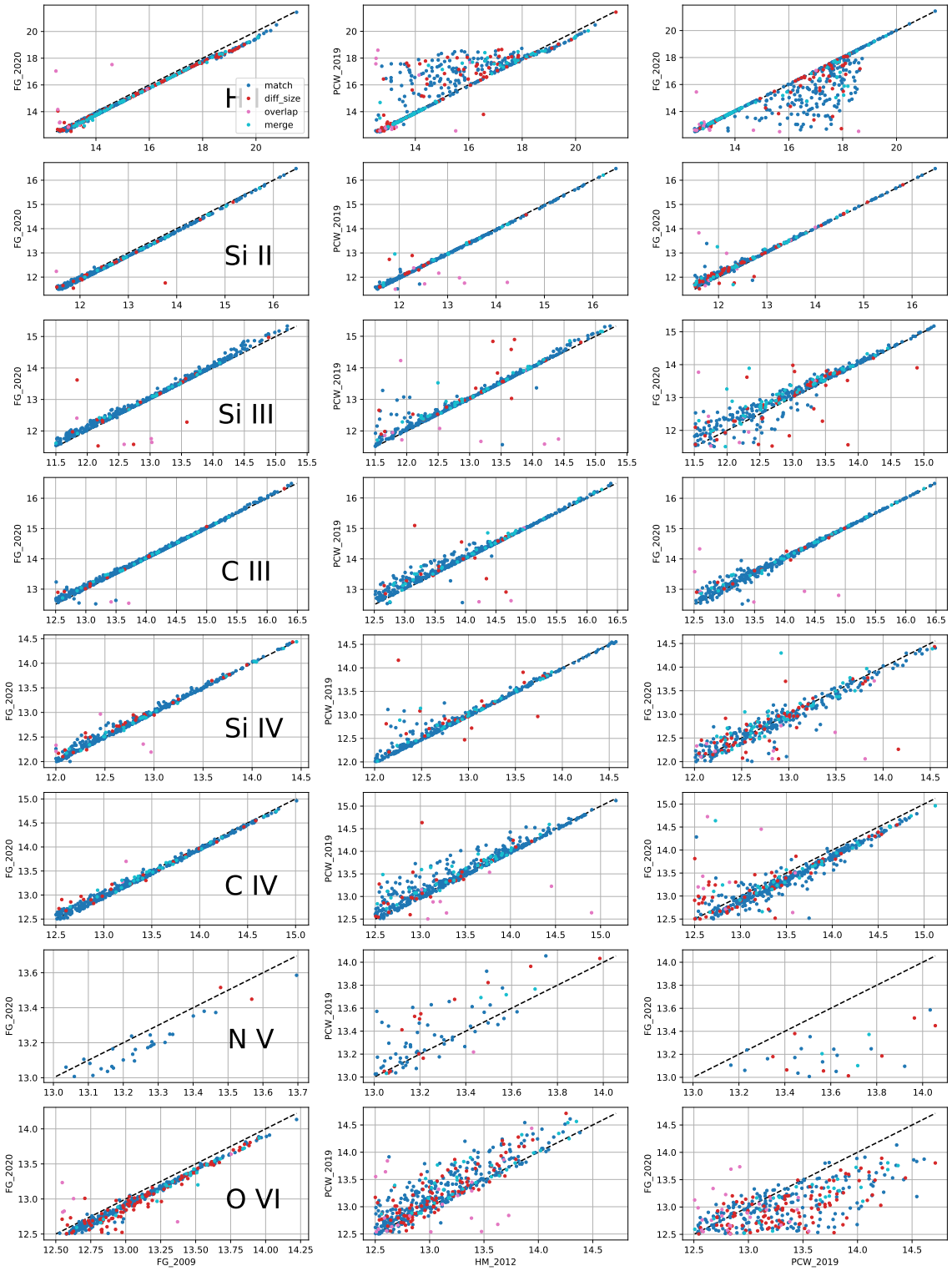

Figure 6: Direct absorber comparison of column for each pairwise comparisons for each ion in the analysis. The x-axis contains the log column density for absorbers in the older UVB models, while the y-axis contains log column densities of the newer models. The dashed black line at the center of the figure indicates the line of equality between the to models. The pairwise comparisons going from left to right are: FG20 vs FG09, PW19 vs HM12 and FG20 vs PW19. This figure's new, so I haven't began discussing it yet. [BWO: axis labels need to indicate that you're looking at column densities. x- and y-axes in a given row and column do not have the same column density ranges - I think they should all be identical even if you're not showing values below some range for a given species, just so it's easy to interpret what's going on (and so you can get rid of a lot of text/whitespace). Text needs to generally be bigger. Key in the top left panel covers "HI" and that needs to be fixed – I think you can move the ion labels to the top left corner of those panels without hiding any information.]

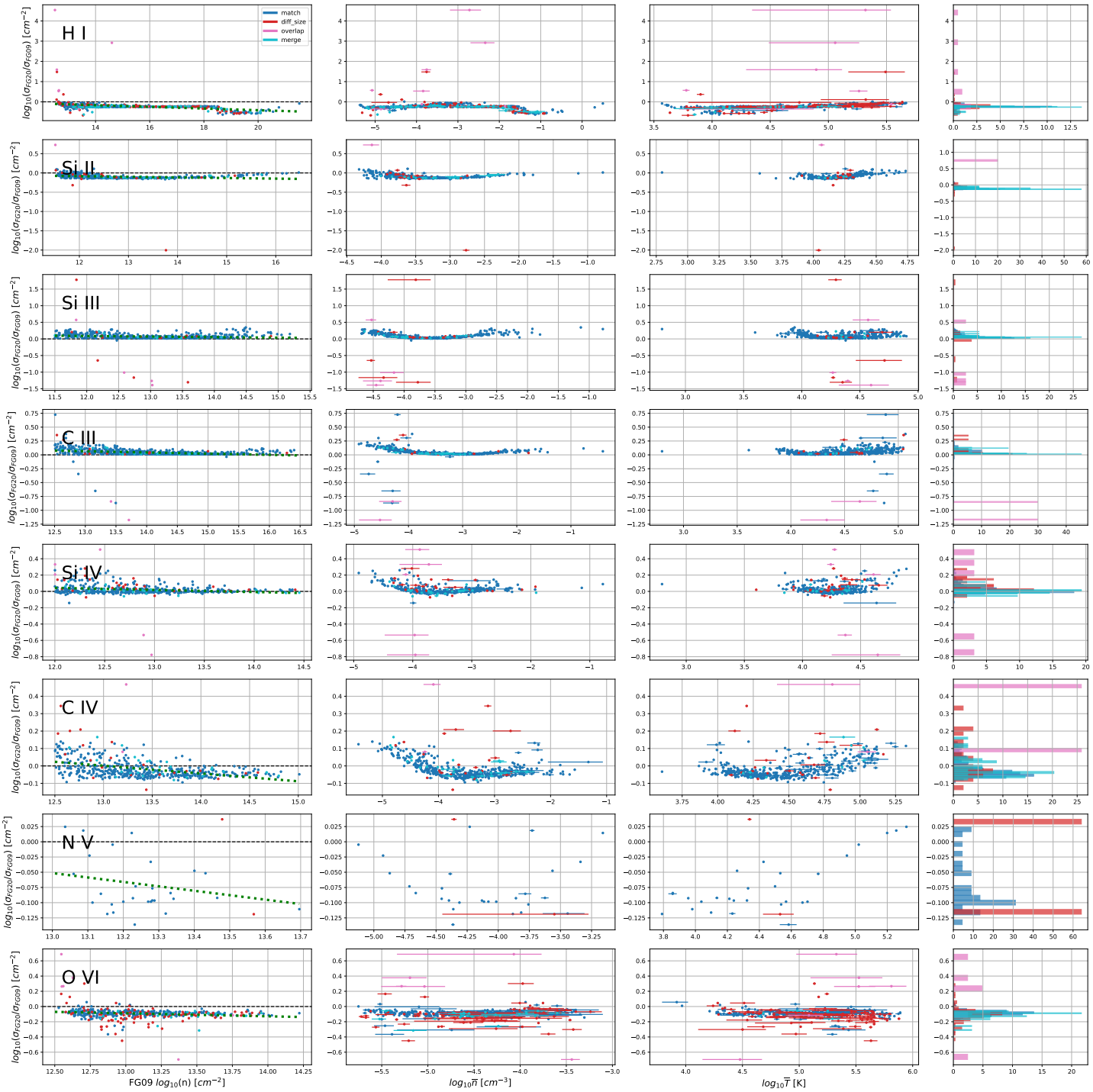

Figure 7: Comparison between the SALSA absorbers from the FG 2009 and FG 2020 UVB models based on their column density, temperature and gas density. The leftmost column is a direct comparison between column densities with FG 2009 column densities in the x-axis and FG 2020 in the y-axis. [BWO: the previous sentence is not true.] A dashed black line is included to represent the "match" line where the two absorber column densities match with one another. Additionally, a green dotted line is included as a linear fit generated to the comparison scatter. The second column shows the gas density comparison, where the x-axis is the average gas density (n) between the two UVB models with error bars showing the lower and higher densities. On the y-axis is the $\log_{10}$ ratio between FG20 / FG09. The third column is the temperature comparison where the x-axis is the average temperature with error bars showing the smaller and larger values of temperature and the y-axis is once again the $\log_{10}$ ratio between FG 2020 / FG 2009. The final column is a histogram showing the distribution of the FG 2020–FG 2009 ratio. Each row is a different ion used in the analysis, and each point is colored based on their spatial relation to one another as outlined in Section 2.6. [BWO: There is a lots of duplicative text in the figure - we've talked about how to remove this. Axis label text needs to be bigger so it's easier to read. I would suggest making column densities and other quantities in each column the same so that it's easier to interpret, even if there is more whitespace in a given panel.]

column. Each row represents a different ion as indicated by the label in the panels in the leftmost column, listed in order of increasing species ionization potential.

In H I, we see that ions using the FG 2020 UVB have systematically lower column densities than with FG 2009. Notably, at gas number density $\log n = -1$, the difference between the two UVBs increases to a maximum of ~ 0.5 dex. This difference appears to be associated with lower temperature absorbers ($\sim \log(T)$ =4.0-4.5 K) as can be seen in the third column. In fact, most of the H I absorbers with larger FG09 column densities, tend to be associated with temperatures lower than $\log(T)$ =5 K. Si II, Si III, C III, Si IV and C IV all have very similar trends to one another, at $\leq \log \overline{n} = -4$, FG20 tends to have higher densities that has a downward trend towards until $\sim \log \overline{n} = -4$ after which the UVB absorbers have similar column densities, staying around 0. Si II, while mostly following these trends, appears to be shifted downwards by 0.125 dex. In some of the other lower ionization-state ions, Si IIIand C III, we see that around $\log \overline{n} = -3$, there is an upwards trend where FG20 has higher column densities. The density remains around 0 in Si IVand C IV. There are no noticeable trends with temperature except for C IV, where FG20 tends to have higher densities at $\geq \log \overline{T} = 4.625$ There are very few N V absorption systems and thus it is very difficult to extract a trend from this species. It does appear, however, that the absorbers SALSA does identify have very similar column densities to one another. There is a faint trend with $\overline{T}$ where ¿$\log \overline{T} = 4.6$ tends to have more similar column densities as temperature increases. Finally, O VI has no trends with gas density or temperature, but the FG09 UVB does have systematically higher column densities by a factor of $\simeq 0.1$ dex.

Fig. 8 is a very similar plot to Fig. 7 now with the comparison being between PW19 and HM12 with the column density ratio being $\sigma_{PW19}/\sigma_{HM12}$. [BWO: You don't mention the σ stuff for the previous figure; I think it's good to define it, so I would suggest going back to the previous figure description and defining it there too.]

For H I, we see from $\log \overline{n} = -4$ to -1.5 that there are significant differences between the two UVBs. While absorbers typically have similar column densities (with better agreement at higher column) there is significant scatter at relatively low column densities, with a moderate but notable fraction of PW19 absorbers having column densities larger by several dex than their HM12 counterparts. Based on columns two and three, these differences are most pronounced in absorbers with intermediate densities and high temperatures ($\log \overline{T} > 4.25$). Excluding Si II, which does not appear to have many significant differences between the two UVBs, the Si and C ions both show significant column density differences at $\log \overline{n} < -4$, after which the column density differences tend to stay around 0. While Si ion column density differences become less significant with increasing $\overline{n}$, C ion column densities with $\log \overline{n} = -4.25$ have larger column density differences peaking at 0.5 dex for C IIIand 0.75 dex for C IV. As with Fig. 7, are relatively few N V absorbers and thus it is very difficult to extract any useful trend from these panels. O VI, however, displays a notable trend with gas density. Above $\log \overline{n} = -4.5$, the column density difference immediately scatters with many PW19 absorbers having significantly larger differences that range from 0 to 0.6 dex. There are no notable trends with HM12 column density or $\overline{T}$.

Fig. 9 is similar to the previous two figures, but now comparing PW19 and FG20 with a column density ratio of $\sigma_{PW19}/\sigma_{FG20}$.

The H I absorbers show a similar feature as seen in Fig. 8 from $\log \overline{n} = -4$ to -1.5, with a maximum difference of approximately 4 dex. This structure is also reflected in Column 3, where the absorbers with larger column density differences generally exist at $\log \overline{T} > 4.25$. Si III, C III, Si IV and C IV, as in Fig. 8, have very little column density differences except for $\log \overline{n} < -4$ where the scatter becomes significantly larger. As with previous comparisons, the number of N V absorbers are low and thus trends are difficult to discern. O VI has overall very high scatter between the two UVBs, but it does appear that as gas density increases the column density difference grows larger in favor of PW19.

It should also be noted that in addition to examining ion number density and temperature differences for each species we also looked for trends relating to variation in metallicity. We did not find any discernible trends relating to metallicity for any of the ions considered in this work, and thus for the sake of clarity we have not showed those results in the figures presented here.

4. DISCUSSION

In this experiment we have used the Trident and SALSA software packages to create and analyze 100 randomly-oriented lines of sight through the circumgalactic medium of a simulated Milky Way progenitor galaxy from the FOGGIE project and to extract absorbers from each ray assuming four different metagalactic ultraviolet backgrounds from two different families of models (Faucher-Giguère 2009, Faucher-Giguère 2020, Haart & Madauu 2012 and Puch-

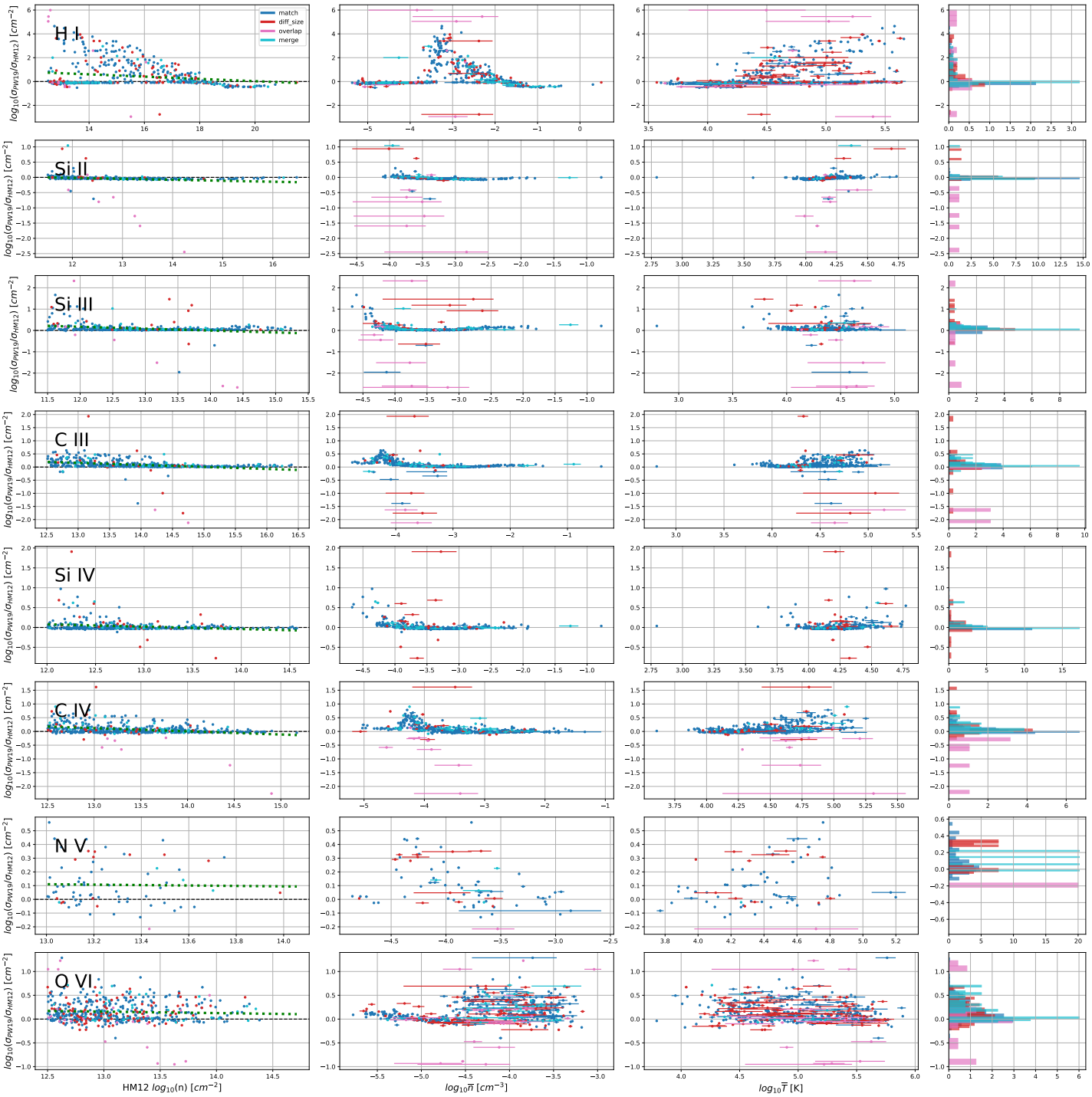

Figure 8: Similar to Fig. 7, now comparing HM12 and PW19. The ratio between the two is $\sigma_{PW19}/\sigma_{HM12}$. [BWO: Same coments apply as to the previous figure; I think you can make it a lot easier to interpret these results by making axes within a row or column identical (y-axis usually is identical in a row; x-axis in a column typically varies a lot and thus is confusing to interpret). One particular point about the HI panels is that for the ones where there is a many-dex difference it's unclear to me that averaging the two column densities together is totally logical. I'm not sure if there's a better way to do it, but it does mean that location on the x-axis is somewhat unclear...]

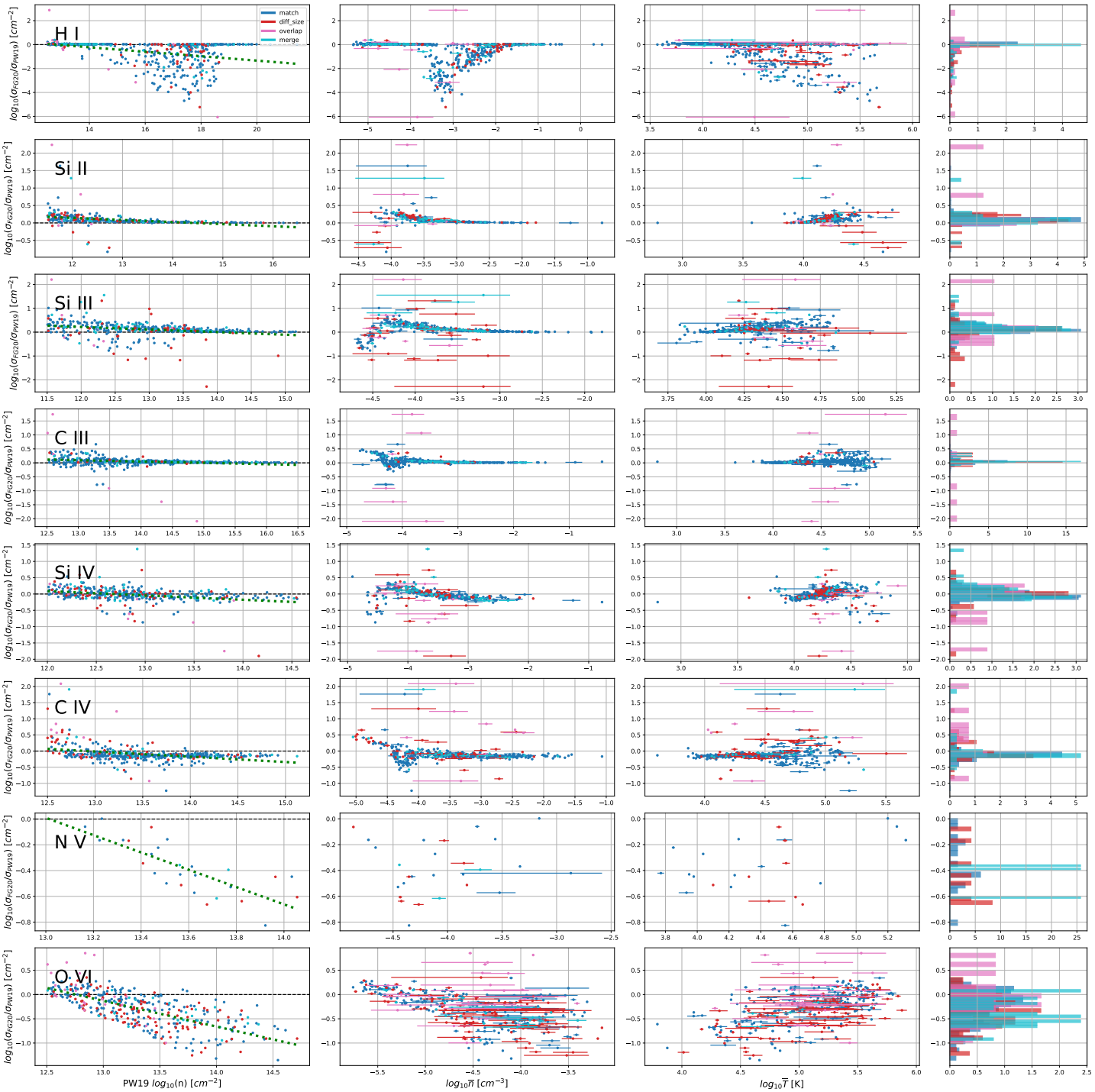

Figure 9: Similar to Fig. 7 and Fig. 8, now comparing FG20 and PW19. The ratio between the two is $\sigma_{PW19}/\sigma_{FG20}$. [BWO: Same comments apply to this as to previous figures.]

wein et al. 2019). We then performed three pairwise comparisons (FG09 to FG20, HM12 to PW19 and PW19 to FG20) examining the evolution of these model families as well as comparison between the most current version of these models for eight different ions (H I, Si II, Si III, C III, Si IV, C IV, N V, and O VI). We then examined differences in column density for entire lines of sight as well as individual absorbers, with a particular focus on the differences relating to the physical conditions of the absorbers.

4.1. *Interpretation of results*

Many–but not all–of the results presented in Section 3 can be understood by differences in the overall magnitude of the metagalactic ultraviolet background at the ionization energies corresponding to the ions under consideration, as shown in Figure 2. Figure 5 shows ray-by-ray comparison of the total column density of each ion. In general, species where the magnitude of the UVB flux at the ionization potential vary significantly (such as H I, N V, or O VI) show significant offsets between the total amount of each ion, whereas species where the UVB flux magnitudes are much closer at the ionization energy (e.g., Si III) tend to show correspondingly smaller systematic offsets. Within these results, however, some lines of sight have extremely large column density differences (up to a few orders of magnitude for H I and Si II over a narrow range of total column density). Absorber-by-absorber comparisons (in Figures 7-9) suggest that this has to do with differences at relatively specific ranges of species number density and temperature, which require further examination. It is possible that this is because each species that we consider reaches its equilibrium by a combination of UV background-driven processes (i.e., photoionization both into and out of the ion in question) and collisional processes (both ionization and recombination). These processes depend on a complex combination of gas density and temperature as well as the properties of the metagalactic UV background, and these nonlinear interactions must be the cause of the differences that we see. [BWO: I think we actually need to look at the species fractions as a function of density and temperature that come out of CLOUDY and compare those to each other! That will help to make sense of this. Let's discuss.]

For the SALSA-extracted absorber pairs (Figures 7-9), we find that the trends in our results tend to make sense given the combination of photoionization- and collisionally-driven reactions that control the ion balance at a given point in thermodynamic phase space. The scatter in column density ratio tends to increase with increasing species ionization energy, which makes sense because the metagalactic ionizing background is relatively poorly constrained at those high energies and thus the models vary substantially in their predictions for the UVB flux. This translates into significant differences in the region of temperature-density phase space where one would expect photoionization processes to dominate over collisional processes–as the magnitude of the UVB goes up, this should happen at proportionally higher densities and lower temperatures. The relatively narrow bands of number density where significant differences occur can be understood in this way. Consider, for example, the differences observed in H I column density between the HM12 and PW19 UV backgrounds in Figure 8. At low number densities photoionization processes are dominant and at high number densities collisional processes are dominant, regardless of the UV background. Gas at intermediate number densities ($\log N \sim -4$ to -2) and relatively high temperatures ($\log T \geq 4.3$) will be most affected by the shape and magnitude of the UV background near (and slightly below) 13.6 eV. Even given these differences, we find that the vast majority of absorber pairs that were classified as a "match" (as defined in Section 2.6) tend to agree well between the two models being compared in terms of column density, gas density, and temperature. The most egregious outliers that we find do not fall into the "match" category. These outlying absorbers occupy different numbers of cells and positions along the line of sight, and thus tend to be in the "overlap" category – i.e., they are absorbers identified by the SALSA code that have some partial overlap in their physical extent, but only a small fraction of the total column density is overlapping. It is possible that a different approach to identifying absorbers would mitigate or remove these poorly-matched features entirely.

4.2. *Comparison to other work*

The vast majority of work examining the uncertainties in circumgalactic medium absorption line features come from observationally-focused efforts and thus focus on reverse modeling rather than the forward modeling approach that we have taken. One study is from Lehner & Howk (2011), who allow the power-law slope of the metagalactic UV background to vary as a free parameter. Doing so causes uncertainties in CGM ion column densities to increase from 0.08 to 1.14 dex. [BWO: You need to give more information here – which species are they looking at? Over what energy range are they allowing the spectrum to vary?] Our work generally agrees with Lehner et al. in terms of the magnitude of uncertainty, with the majority of uncertainties in the species we consider (outside of H I) remaining within 1 dex. [BWO: Also talk about the Werk+ 2014 or 2015 paper! This is another important observational paper, and specifically a COS-halos paper.]

Mallik et al. (2023) explores a similar scope of questions as those that we address in this work. These authors perform utilize both a forward and backward modeling approach and look at the impact of the metagalactic NV background on simulated absorption features and their subsequently inferred column densities rather than directly looking at the absorbers themselves. Although this leads to more sources of uncertainty, it also produces results that

are more directly comparable to observation. Our work complements the findings of Mallik et al. (2023) by showing that the uncertainty in metal absorbers exists not only through the forward and backward modeling approach taken in their paper, but by examining the impact of the UVB on the physical state of the gas. This changes the ionization state of the gas, impacting the physical extent and overall quantity of each species. Another work, Acharya & Khaire (2022), also finds similar results in their study. This work also employs reverse modeling techniques via the creation of "toy" absorbers, using CLOUDY to recover the H I number density and metallicity. They find similar results to our work, with the main differences being the authors only used H I in their analysis and had a much more significant focus on inferred physical quantities such as density and temperature as opposed to the impact on column density. Our work serves to extend the results of this paper, showing that the variance between the different UVB models result in differences for multiple ion species in both forward modeling and backward modeling approaches. In contrast of these backward modeling approaches, Marra et al. (2023) finds that there is some caution to be had with this methodology and the assumption that all of the absorption features of a cloud originate from a singular absorber. I don't know what the previous sentence means – can you rephrase it? In their work, they found that a significant portion of the features of absorption spectra appear from sets of multiple absorbers, a significant portion of which do not share common gas mass. [BWO: What do you mean by "common gas mass"? Do you mean that they come from multiple distinct physical components of the gas?] This serves to support our forward modeling approach as we are completely able to avoid introducing the uncertainty from this assumption into our analysis.

Another study that analyzes the CGM at $z \approx 2$, Lehner et al. (2022), analyzes the metallicity of CGM absorbers observed by KODIAQ-Z as compared to FOGGIE simulation data. To extract absorbers from the FOGGIE galaxies the authors also use the Trident and SALSA codes, using HM 2012 as the UV background for their analysis. Given the insights of our work the metallicity in their analysis would likely remain relatively unchanged, regardless of which UVB model was used. However, there would likely be some changes in the H I column densities in the range of $\sim 10^{18} - 10^{20}$ cm^{-2}, as the more recent UVB models predict significantly lower gas densities of H I (≈ 0.5 dex) in this column density range.

4.3. *Limitations and future work*

One of the primary limitations of this work stems from our assumption that absorbers are physically contiguous systems, which is inherent to the absorber-finding algorithm embodied by the SALSA code. While this allows us to extract absorber column densities directly from the FOGGIE simulation data rather than estimating it by analyzing synthetic absorption spectra it does not allow for physically distinct structures with different line-of-sight velocities to contribute to a single absorption feature. This means that there is a gap in realism between our absorbers and observed features. That said, the goal of our work is not to be as physically realistic as possible – our goal is ultimately to compare the impact of different UVB models on a variety of commonly-observed ions in the circumgalactic medium, and the method we have chosen allows us to directly probe the physical impact of these backgrounds on the absorbing gas itself without any confusion relating to the blending of different physical features.

An additional limitation relates to the cutoff fraction and minimum column density variables used in the SALSA code's iterative absorber-finding algorithm (see Section 2.5). While the impact of these parameter values were quantified and values were chosen that provided sensible results, this is still a tunable parameter. Future work may include calibrating these quantities against observational data to further increase accuracy. There is also the use of Boolean logic in the absorber categorization script where the margins of error for establishing these categories are set somewhat arbitrarily. This is further complicated by the varied physical sizes of each cell along the randomly-oriented ray objects (see Section 2.2), which lowers the accuracy of setting a single error margin based around ray cells because each ray cell is not the same size, nor are cells necessarily the same size between different rays. Future studies should attempt to remedy these issues by instead setting an error region based on physical size or some other physical parameter rather than simulation cell counts.

Finally, we note that our post-processing of the FOGGIE simulation data with different metagalactic ultraviolet backgrounds is not entirely physically consistent. These simulations were run using the Haardt & Madau (2012) UVB, and thus have values of density and temperature that evolve under that model assumption. When we post-process the simulation data we use the baryon temperature, density, and metallicity fraction values that ceom from the dataset but we then calculate species ionization fractions using one of the four UV backgrounds. This means that the density and temperature values in particular are not completely consistent with the UV background. A more nominally self-consistent way to approach this would be to run multiple simulations, each with different UV backgrounds. This

would have some impact on the dynamical evolution of the system, however, and due to the inherently chaotic nature of galaxy evolution this would mean that we would not be able to find identical physical structures in each of the simulations. As a result, the approach that we have taken is the only realistic way to perform absorber-by-absorber matching.

There are several additional avenues of future work. One concerns the variation of elemental abundances in the circumgalactic medium. In this work we have implicitly assumed that all gas in the circumgalactic medium, regardless of metallicity, has a Solar abundance pattern. This is not always true, particularly at lower metallicities and at high redshifts. In fact, we would expect that the (non-hydrogen) elements that are commonly observed in the CGM would have some variation in their relative abundance – carbon comes from both exploding massive stars (i.e., Type II supernovae) and from low-mass stars, whereas oxygen and magnesium come entirely from massive stars. Even the elements that come from the same sources will not necessary end up with precisely the same ratios. Furthermore, there is a delay between enrichment from Type II and Type Ia supernovae that will significantly impact the relative contributions of various alpha and iron peak elements. This uncertainty in the chemical composition of the circumgalactic medium will itself contribute to systematic uncertainties in the determination of its overall metallicity beyond those relating to the uncertainty in UV background. Future work will revisit the experiment presented in this paper using different abundance patterns that could potentially more accurately represent that which might be observed in the CGM. We also note that we do not consider the inclusion of the variation of the UV background near galaxies due to the massive stars in that galaxy. This is potentially important in calculating the ionization state of gas that is in the inner CGM (see, e.g., Werk et al. 2016), and it likely also depend on the azimuthal angle – i.e., UV light from stars is going to preferentially escape along the Galactic poles rather than along the equatorial plane. This is also a clear area for future work. Finally, including the line-of-sight velocity of absorbsers in our absorber-finding algorithm is an additional step towards direct comparison to observational results, as this is one of the major limitations of the SALSA algorithm's approach.

5. CONCLUSIONS

In this paper we examine the uncertainties in the column densities of physically-contiguous absorption systems that come from variation in assumptions relating to the metagalactic ultraviolet background. We do this using a "forward modeling" approach where "pencil beams" of physical quantities are extracted from the circumgalactic medium of high resolution cosmological simulations of galaxy evolution from the FOGGIE project, different UV background models are applied to calculate the densities of commonly-observed ions (H I, Si II, Si III, Si IV, C IV, N V, and O VI), and physically contiguous structures are identified. We perform comparisons between pairs of ultraviolet backgrounds, categorize the outcomes, and examine the relationship between the degree of agreement between absorbers of different column densities as a function of UV background and the thermodynamic state of the underlying gas.

We find that matched absorption structures show significant differences based on the choice of ultraviolet background, with notable trends between model generations, model families, and across ions of different ionization energies. Notably, the Puchwein et al. (2019) model tends to produce significantly more H I, C IV, N V, and O VI compared to both its older Haardt & Madau (2012) parent model and to Faucher-Giguère (2020), whereas both generations of the Faucher-Giguère family of models produce comparable amounts of these ions. All of the models produce similar amounts of Si II, Si III, Si IV, and C III.

Similar trends are observed when doing absorber-by-absorber comparisons. Only small ($\lesssim$ 0.1 dex) differences between matched absorbers are seen when comparing within the Faucher-Giguère family of models. When comparing the models within the Haardt-Madau-Puchwein family (and between the two families of models) the most striking differences are seen in absorbers of relatively low column densities (particularly for H I, C IV, and O VI). Examination of the mean density and temperature of the gas producing these ions suggests that the largest differences occur at intermediate densities and relatively temperatures, where variations in the UV background would be most impactful.

The authors thank E. Puchwein for sharing information about UV backgrounds. ET, CK, and BWO acknowledge support from NSF grants #1908109 and #2106575 and NASA ATP grants NNX15AP39G and 80NSSC18K1105. This work used the Extreme Science and Engineering Discovery Environment (XSEDE), which is supported by National Science Foundation grant number TG-AST090040, as well as the resources of the Michigan State University High Performance Computing Center (operated by the MSU Institute for Cyber-Enabled Research). Computations described in this work were performed using the publicly-available YT (Turk et al. 2011), Trident (Hummels et al. 2017), and SALSA (Boyd et al. 2020) codes, which are the products of the collaborative effort of many independent scientists from numerous institutions around the world. This paper uses data from the Figuring Out Gas and Galaxies In Enzo project (FOGGIE; Peeples et al. 2019, and https://foggie.science). We thank the members of the FOGGIE collaboration for sharing this data. [BWO: MOLLY AND JASON – do you think this acknowledgment is appropriate or should we delete it?]

Software: astropy (Astropy Collaboration et al. 2013, 2018), yt (Turk et al. 2011), Trident (Hummels et al. 2017), SALSA (Boyd et al. 2020)

REFERENCES

Acharya, A., & Khaire, V. 2022, Monthly Notices of the Royal Astronomical Society, 509, 5559–5576, doi: 10.1093/mnras/stab3316

Astropy Collaboration, Robitaille, T. P., Tollerud, E. J., et al. 2013, A&A, 558, A33, doi: 10.1051/0004-6361/201322068

Astropy Collaboration, Price-Whelan, A. M., Sipőcz, B. M., et al. 2018, AJ, 156, 123, doi: 10.3847/1538-3881/aabc4f

Berg, M. A., Howk, J. C., Lehner, N., et al. 2019, doi: https://doi.org/10.3847/1538-4357/ab378e

Bordoloi, A. D., & Longmire, E. K. 2018, Physical Review Fluids, 3, doi: 10.1103/physrevfluids.3.123602

Bordoloi, R., Lilly, S. J., Kacprzak, G. G., & Churchill, C. W. 2014, ApJ, 784, 108, doi: 10.1088/0004-637X/784/2/108

Boyd, B., Silvia, D., O'Shea, B., et al. 2020, The Journal of Open Source Software, 5, 2581, doi: 10.21105/joss.02581

Burchett, J., Tripp, T., Prochaska, J., et al. 2018, doi: 10.48550/arXiv.1810.06560

Butsky, I. S., Werk, J. K., Tchernyshyov, K., et al. 2022, The Astrophysical Journal, 935, 69, doi: 10.3847/1538-4357/ac7ebd

Chen, H.-W., Zahedy, F. S., Boettcher, E., et al. 2020, Monthly Notices of the Royal Astronomical Society, 497, 498

DeFelippis, D., Bouché, N. F., Genel, S., et al. 2021, The Astrophysical Journal, 923, 56, doi: 10.3847/1538-4357/ac2cbf

Faucher-Giguère, C.-A. 2020, MNRAS, 493, 1614, doi: 10.1093/mnras/staa302

Faucher-Giguère, C.-A., Lidz, A., Zaldarriaga, M., & Hernquist, L. 2009, ApJ, 703, 1416, doi: 10.1088/0004-637X/703/2/1416

Fielding, D., Quataert, E., McCourt, M., & Thompson, T. A. 2017, Monthly Notices of the Royal Astronomical Society, 466, 3810–3826, doi: 10.1093/mnras/stw3326

Gibson, J. L., Lehner, N., Oppenheimer, B. D., et al. 2022, The Astronomical Journal, 164, 9, doi: 10.3847/1538-3881/ac69d0

Haardt, F., & Madau, P. 2012, ApJ, 746, 125, doi: 10.1088/0004-637X/746/2/125

Haislmaier, K., Tripp, T., Katz, N., et al. 2020, Monthly Notices of the Royal Astronomical Society, 502, doi: 10.1093/mnras/staa3544

Hummels, C. B., Smith, B. D., & Silvia, D. W. 2017, ApJ, 847, 59, doi: 10.3847/1538-4357/aa7e2d

Hummels, C. B., Smith, B. D., Hopkins, P. F., et al. 2019, ApJ, 882, 156, doi: 10.3847/1538-4357/ab378f

Lehner, N., & Howk, J. C. 2011, Science, 334, 955–958, doi: 10.1126/science.1209069

Lehner, N., O'Meara, J., Fox, A., et al. 2014, The Astrophysical Journal, 788, doi: 10.1088/0004-637X/788/2/119

Lehner, N., O'Meara, J. M., Howk, J. C., Prochaska, J. X., & Fumagalli, M. 2016, ApJ, 833, 283, doi: 10.3847/1538-4357/833/2/283

Lehner, N., Wotta, C. B., Howk, J. C., et al. 2018, The Astrophysical Journal, 866, 33, doi: 10.3847/1538-4357/aadd03

Lehner, N., Kopenhafer, C., O'Meara, J., et al. 2022, The Astrophysical Journal, 936, 156, doi: 10.3847/1538-4357/ac7400

Mallik, S., Srianand, R., Maitra, S., Gaikwad, P., & Khandai, N. 2023, Monthly Notices of the Royal Astronomical Society, 523, 2296, doi: 10.1093/mnras/stad1550

Marra, R., Churchill, C., Kacprzak, G., et al. 2023, Monthly Notices of the Royal Astronomical Society, 527, doi: 10.1093/mnras/stad3735

Marra, R., Churchill, C. W., Kacprzak, G. G., et al. 2022, Examining quasar absorption-line analysis methods: the tension between simulations and observational assumptions key to modelling clouds. https://arxiv.org/abs/2202.12228

Marra, R., Churchill, C. W., Doughty, C., et al. 2021, MNRAS, 508, 4938, doi: 10.1093/mnras/stab2896

Oñorbe, J., Hennawi, J. F., Lukić, Z., & Walther, M. 2017, ApJ, 847, 63, doi: 10.3847/1538-4357/aa898d

Peeples, M. S., Corlies, L., Tumlinson, J., et al. 2019, The Astrophysical Journal, 873, 129, doi: 10.3847/1538-4357/ab0654

Prochaska, J. X., Macquart, J.-P., McQuinn, M., et al. 2019, Science, 366, 231–234, doi: 10.1126/science.aay0073

Puchwein, E., Haardt, F., Haehnelt, M. G., & Madau, P. 2019, Monthly Notices of the Royal Astronomical Society, 485, 47, doi: 10.1093/mnras/stz222

Ramesh, R., Nelson, D., Fielding, D., & Brüggen, M. 2024, Astronomy amp; Astrophysics, 684, L16, doi: 10.1051/0004-6361/202348786

Schaye, J., Crain, R. A., Bower, R. G., et al. 2014, Monthly Notices of the Royal Astronomical Society, 446, 521–554, doi: 10.1093/mnras/stu2058

Simons, R. C., Peeples, M. S., Tumlinson, J., et al. 2020, ApJ, 905, 167, doi: 10.3847/1538-4357/abc5b8

Tumlinson, J., Thom, C., Werk, J. K., et al. 2011, Science, 334, 948–952, doi: 10.1126/science.1209840

Tumlinson, J., Thom, C., Werk, J. K., et al. 2013, ApJ, 777, 59, doi: 10.1088/0004-637X/777/1/59

Turk, M. J., Smith, B. D., Oishi, J. S., et al. 2011, ApJS, 192, 9, doi: 10.1088/0067-0049/192/1/9

Werk, J. K., Prochaska, J. X., Tumlinson, J., et al. 2013, The Astrophysical Journal, 792, 8, doi: 10.1088/0004-637x/792/1/8

Werk, J. K., Prochaska, J. X., Cantalupo, S., et al. 2016, The Astrophysical Journal, 833, 54, doi: 10.3847/1538-4357/833/1/54

Wijers, N. A., Schaye, J., & Oppenheimer, B. D. 2020, The warm-hot circumgalactic medium around EAGLE-simulation galaxies and its detection prospects with X-ray and UV line absorption. https://arxiv.org/abs/2004.05171

Wilde, M. C., Werk, J. K., Burchett, J. N., et al. 2021, The Astrophysical Journal, 912, 9, doi: 10.3847/1538-4357/abea14

Yaman, F., Yakhno, V. G., & Potthast, R. 2013, Mathematical problems in engineering, 2013, 976837

Zheng, Y., Peeples, M. S., O'Shea, B. W., et al. 2020, The Astrophysical Journal, 896, 143, doi: 10.3847/1538-4357/ab960a